SCIENTIFIC REPORTS

OPEN

Near-infrared induced phase-shifted ICG/Fe_3O_4 loaded PLGA nanoparticles for photothermal tumor ablation

Received: 11 April 2017
Accepted: 7 June 2017
Published online: 14 July 2017

Chengcheng Niu[1], Yan Xu[1], Senbo An[2], Ming Zhang[1], Yihe Hu[2], Long Wang[2] & Qinghai Peng[1]

Near-infrared (NIR) laser-induced photothermal therapy (PTT) uses a photothermal agent to convert optical energy into thermal energy and has great potential as an effective local, minimally invasive treatment modality for killing cancer cells. To improve the efficacy of PTT, we developed poly(lactide-co-glycolide) (PLGA) nanoparticles (NPs) encapsulating superparamagnetic iron oxide (Fe_3O_4), indocyanine green (ICG), and perfluoropentane (PFP) as synergistic agents for NIR laser-induced PTT. We fabricated a novel type of phase-shifting fluorescent magnetic NPs, Fe_3O_4/ICG@PLGA/PFP NPs, that effectively produce heat in response to NIR laser irradiation for an enhanced thermal ablation effect and a phase-shift thermoelastic expansion effect, and thus, can be used as a photothermal agent. After *in vitro* treatment of MCF-7 breast cancer cells with Fe_3O_4/ICG@PLGA/PFP NPs and NIR laser irradiation, histology and electron microscopy confirmed severe damage to the cells and the formation of many microbubbles with iron particles at the edge or outside of the microbubbles. *In vivo* experiments in mice with MCF-7 tumors demonstrated that Fe_3O_4/ICG@PLGA/PFP NPs could achieve tumor ablation upon NIR laser irradiation with minimal toxicity to non-irradiated tissues. Together, our results indicate that Fe_3O_4/ICG@PLGA/PFP NPs can be used as effective nanotheranostic agents for tumor ablation.

Photothermal therapy (PTT) employs a near-infrared (NIR) laser and photo-absorbing agents to generate heat from light energy to "burn" cancer cells[1,2]. Compared with traditional treatments, such as chemotherapy, radiotherapy and surgery, PTT is a less invasive and highly effective therapeutic approach applied for local treatment of tumors. With high intensity focused ultrasound (HIFU) ablation, the high acoustic power may cause severe side effects in normal tissue in the ultrasound propagation channel because a high temperature can be generated in any tissue, not only in the presence of the nanoparticles. In contrast, for PTT to generate a high temperature in tissues, the photo-absorbing nanoparticles must be present, and thus, the effect more accurately damages the targeted legions[3,4]. Several nanomaterials with excellent NIR light absorption properties have been developed as PTT agents, including gold nanomaterials[5–12], copper nanomaterials[13–18], carbon nanomaterials[19–23], and NIR dyes[24–27]. However, the potential toxicity of non-degradable or slowly degradable nanoparticles (NPs), especially carbon nanotubes or gold nanoparticles, will inevitably limit their clinic applications[28–30]. Thus, there is a significant need to develop a biologically safe and biodegradable photoabsorber for the NIR laser-induced PTT.

Indocyanine green (ICG), as the only NIR agent approved by the U.S. Food and Drug Administration (FDA) to date, has been widely used for human clinical NIR fluorescence (NIRF) imaging and diagnosis[31,32]. Several challenges exist with regard to the use of ICG in PTT applications though, such as its instability in aqueous solution, light- and temperature-dependent properties, and rapid blood clearance[33,34]. To overcome these limitations, researchers have developed polymeric NP delivery systems for encapsulating ICG[35,36]. Several studies have shown that encapsulation of ICG in NPs can enhance the stability of ICG for *in vivo* NIRF imaging and increase its accumulation in tumors through an "enhanced permeability and retention effect" (EPR effect)[37–40]. Therefore, the efficacy of PTT can be enhanced by the use of NP-encapsulated ICG.

[1]Department of Ultrasound Diagnosis, The Second Xiangya Hospital, Central South University, Changsha, Hunan, 410011, China. [2]Department of Orthopedics, Xiangya Hospital, Central South University, Changsha, Hunan, 410008, China. Correspondence and requests for materials should be addressed to L.W. (email: dr_wanglong@csu.edu.cn) or Q.P. (email: pqh12079@aliyun.com)

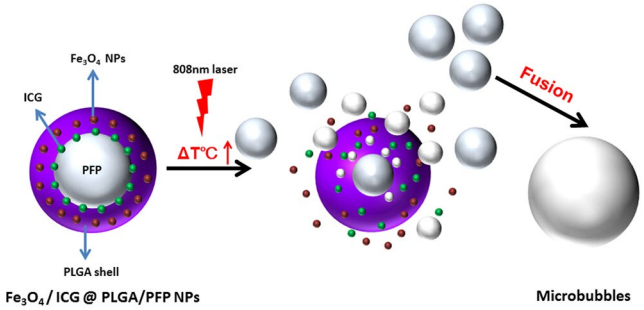

Figure 1. Schematic illustration of the structure of Fe_3O_4/ICG@PLGA/PFP NPs and the progress of the generation of mircobubbles from within the NPs via NIR-induced vaporization of PFP.

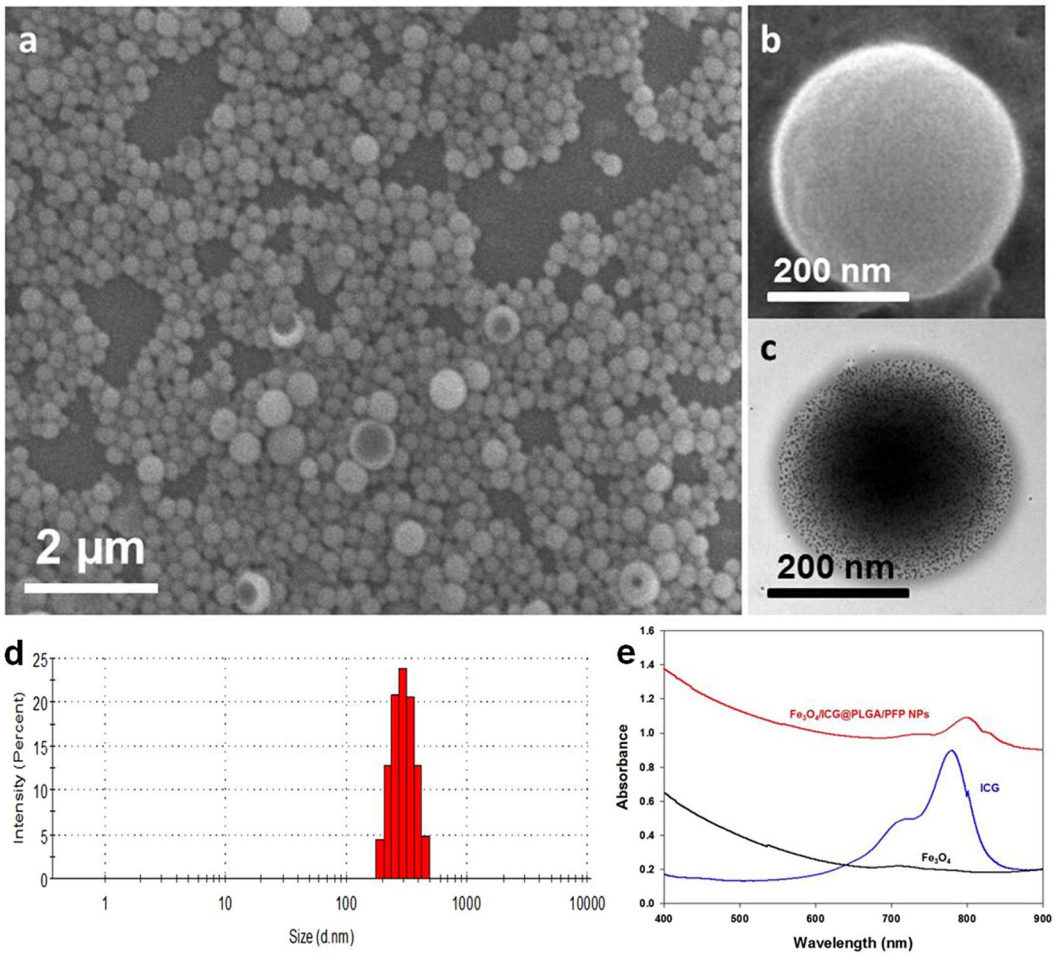

Figure 2. (**a**,**b**) SEM images of Fe_3O_4/ICG@PLGA/PFP NPs (**a**) 10000×; scale bar, 2 μm; (**b**) 70000×; scale bar, 200 nm); (**c**) TEM image of Fe_3O_4/ICG@PLGA/PFP NPs with a large amount of black Fe_3O_4 NPs embedded in the spherical shell (70000×; scale bar, 200 nm); (**d**) size distribution of Fe_3O_4/ICG@PLGA/PFP NPs with the average diameter of 289.6 ± 67.4 nm; (**e**) UV-Vis-NIR absorption spectra of Fe_3O_4/ICG@PLGA/PFP NPs, free ICG and Fe_3O_4 NPs.

Magnetic iron oxide (Fe_3O_4) NPs have received great attention for their low toxicity, strong effects on T_2 and T_2^* relaxation for magnetic resonance imaging (MRI), and excellent photo-absorbing ability[1,2,41,42]. However, individual magnetic nanoparticles are susceptible to opsonization in the bloodstream, which will lead to uptake by the reticuloendothelial system (RES) and quick clearance from the blood, resulting in limited distribution in target tissue[43,44], and thereby hindering the imaging or PTT efficacy. Many polymers systems have been investigated for use in decorating the magnetic NPs to address this issue[45,46]. Poly (lactide-co-glycolide) (PLGA) is one of the most widely used polymers for its biodegradability and biocompatibility as well as approval by the FDA.

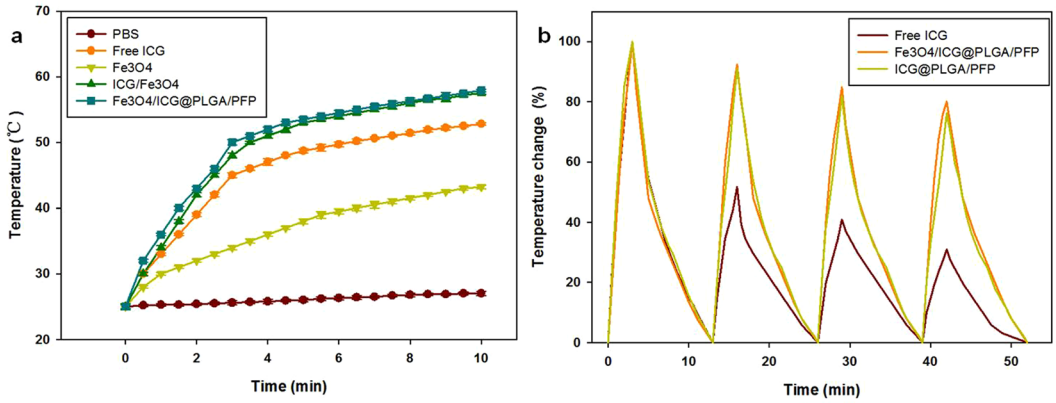

Figure 3. *In vitro* photothermal effects of Fe_3O_4/ICG@PLGA/PFP NPs. (**a**) Temperatures elevation of Fe_3O_4/ICG@PLGA/PFP NPs, mixture of free ICG and Fe_3O_4 NPs, free ICG, Fe_3O_4 NPs, and PBS with continuous NIR laser irradiation (808 nm, 1.0 W/cm^2, 10 min). (**b**) Temperature changes of Fe_3O_4/ICG@PLGA/PFP NPs, ICG@PLGA/PFP NPs, and free ICG over four NIR laser ON/OFF cycles.

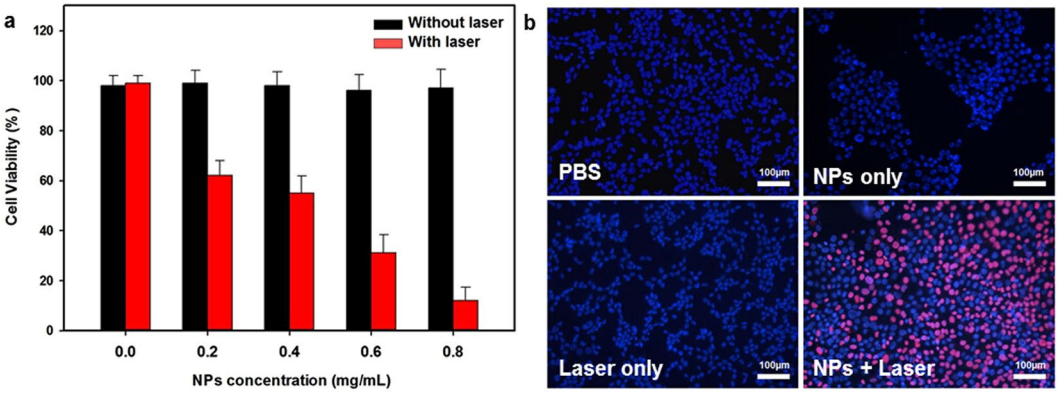

Figure 4. *In vitro* cytotoxicity experiments. (**a**) Relative viability of MCF-7 cells incubated with different concentrations of Fe_3O_4/ICG@PLGA/PFP NPs under laser irradiation (808 nm, 1 W/cm^2, 5 min). (**b**) Fluorescence images of Hoechst 33342/PI co-stained MCF-7 cells incubated with Fe_3O_4/ICG@PLGA/PFP NPs (0.5 mg/mL) and exposed to the 808 nm laser irradiation (1 W/cm^2, 5 min). Live and dead cells were stained with Hoechst 33342 (blue color) and PI (red color), respectively.

Previously, we developed PLGA microbubbles loaded with doxorubicin and Fe_3O_4 NPs and demonstrated their suitability for dual MR/ultrasound (MR/US) imaging of sentinel lymph nodes and their anti-tumor efficacy for lymph node metastasis[47].

Recently, many studies have focused on liquid perfluorocarbon (PFC) droplets, which can be vaporized into gas bubbles via active US sonication or laser irradiation[48,49]. This property of vaporization has been effectively employed for US imaging[50], cancer therapy via vessel occlusion[51–53], targeted drug delivery[54–56], and thermal ablation of tumor cells[57,58]. However, this technology has yet to be combined with a dual NIR light-absorbing agent along with encapsulation in polymeric NPs toward the development of an effective PTT approach.

Here, we report the development of novel pefluoropentane (PFP)-based PLGA NPs loaded with Fe_3O_4 NPs and ICG (Fe_3O_4/ICG@PLGA/PFP NPs) for photothermal tumor ablation (Fig. 1). Both Fe_3O_4 NPs and ICG contribute to the ability of this NIR light-absorbing agent to efficiently convert absorbed light into heat. The liquid PFP core with a lower boiling point is easily converted into gas upon heating to physiological temperatures, and this thermoelastic expansion results in tissue extrusion deformation to enhance the thermal ablation effect in the local tumor area. Our results show that these dual NIR light-absorbing PFC-based polymeric NPs can be used as effective nanotheranostic agents in anti-tumor treatments.

Materials and Methods

Materials. ICG, poly vinyl alcohol (PVA, Mw = 30,000–70,000), and PLGA (lactide: glycolide = 50:50, Mw = 10,000) were obtained from Sigma-Aldrich (USA). Fe_3O_4 NPs (diameter = 10 nm) treated with oleic acid were purchased from Ocean Nano Tech Inc. (USA). PFP was purchased from Alfa Aesar (UK). De-ionized (DI) water was purified using a Milli-Q Gradient System. Other regents of analytical grade were used without further purification. All experiments involving use of animals were performed in accordance with the relevant guidelines

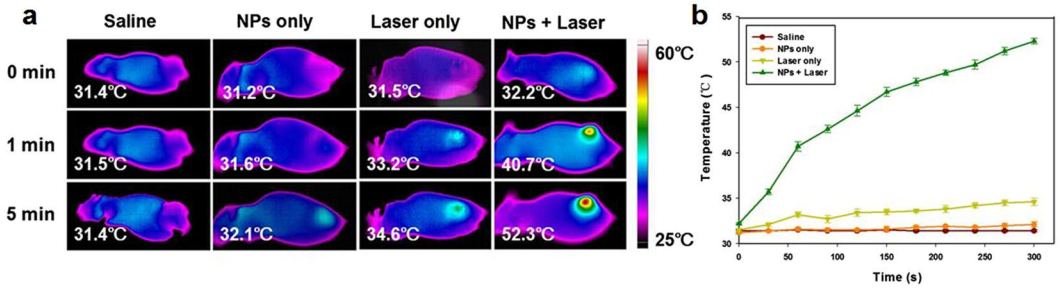

Figure 5. *In vivo* PTT effectiveness of Fe_3O_4/ICG@PLGA/PFP NPs. (**a**) IR thermal images showing the temperature changes in tumors in mice that received different treatments. (**b**) Peak temperature profiles in tumors with different treatments.

and regulations, approved by the Ethics Committee at the second Xiangya Hospital of Central South University in China.

Preparation of Fe_3O_4/ICG@PLGA/PFP NPs. The Fe_3O_4/ICG@PLGA/PFP NPs were fabricated using a slightly modified double emulsion method[47]. Briefly, 500 mg PLGA and 2 mL Fe_3O_4 NPs suspension (31 mg Fe/mL) were added to 10 mL of chloroform and stirred well, and then 2 mL ICG solution (1.25 mg/mL) and 4 mL liquid PFP were added and emulsified for 1 min in an ice bath using an ultrasonic processor. Then 50 mL cold PVA solution (5% w/v) was poured into the emulsion, which was homogenized for 5 min at 9500 rpm in an ice bath using a homogenizer. Subsequently, 100 mL DI water was added to the mixture and mixed for 2 h. Finally, the NPs were washed with DI water three times and kept at 4 °C until characterization. The same procedure was used to prepare Fe_3O_4/ICG@PLGA NPs without PFP, Fe_3O_4 @PLGA/PFP NPs without ICG, and ICG@PLGA/PFP NPs without Fe3O4 as controls.

Characterization of Fe_3O_4/ICG@PLGA/PFP NPs. The morphology of Fe_3O_4/ICG@PLGA/PFP NPs was observed by scanning electron microscopy (SEM, JEOL-7800F). The structure and the presence of Fe_3O_4 NPs in the NP shell were confirmed by transmission electron microscopy (TEM, Hitachi H-7600). The size distribution of NPs was analyzed using a Nano ZS dynamic light scattering analyzer (Malvern Instruments, UK). The amount of elemental Fe encapsulated in the NPs was determined by atomic absorption spectrometry. The UV-Vis-NIR absorption spectra of free ICG, Fe_3O_4 NPs and Fe_3O_4/ICG@PLGA/PFP NPs (0.2 mL of each sample, equivalent ICG concentration of 5 μg/mL and equivalent Fe concentration of 113 μg/mL) were obtained using a steady state spectrophotometer (QuantaMaster™ 40, USA) at room temperature to ensure high absorption in the NIR region and to monitor the ICG content. The encapsulation efficiency of ICG in Fe_3O_4/ICG@PLGA/PFP NPs was calculated as the weight ratio of encapsulated ICG to the total added ICG amount[43]. The amount of encapsulated ICG was calculated as the difference between the total added ICG amount and the amount recovered in washed supernatants during preparation.

Temperature elevation induced by NIR laser irradiation. The temperature profile of Fe_3O_4/ICG@PLGA/PFP NPs was monitored under laser irradiation using an infrared thermometer (Fluke 62 MAX, USA). Aqueous suspensions of Fe_3O_4/ICG@PLGA/PFP NPs, mixture of ICG and Fe_3O_4 NPs, free ICG, Fe_3O_4 NPs, and phosphate-buffered saline (PBS; as the negative control) in wells of a 96-well plate (0.2 mL/well) were irradiated by a NIR 808 nm laser at 1.0 W/cm^2 for 10 min (T808F2W, Xi'an Minghui Optoelectronic Technology, China). The amount of ICG was equivalent in the free ICG, mixture of ICG and Fe_3O_4 NPs, and Fe_3O_4/ICG@PLGA/PFP NPs samples (5 μg/mL ICG)[1,55], and the amount of Fe_3O_4 was equivalent in the Fe_3O_4 NPs, mixture of ICG and Fe_3O_4 NPs, and Fe_3O_4/ICG@PLGA/PFP NPs samples (113 μg/mL Fe). The temperatures of the solutions were measured at 30-s intervals.

Photostability of Fe_3O_4/ICG@PLGA/PFP NPs. The photostability of Fe_3O_4/ICG@PLGA/PFP NPs was tested out under 808 nm NIR laser ON/OFF cycle irradiation. For comparison with free ICG, Fe_3O_4/ICG@PLGA/PFP NPs, CG@PLGA/PFP NPs, and free ICG were irradiated for 3 min (Laser ON), followed by naturally cooling for 10 min (Laser OFF). This ON/OFF cycle was repeated four times, and the temperatures of the solutions were measured at 30-s intervals.

***In vitro* cell experiments.** The cytotoxicity of Fe_3O_4/ICG@PLGA/PFP NPs was evaluated using cell counting kit (CCK-8) assays with the human breast cancer MCF-7 cell line. MCF-7 cells (10^4 cells/well) were incubated in 96-well plates at 37 °C for 24 h. Different dosages (0.2, 0.4, 0.6 and 0.8 mg/mL, 0.1 mL/well) of Fe3O4/ICG@PLGA/PFP NPs suspension were added for incubation for 6 h. Medium without Fe_3O_4/ICG@PLGA/PFP NPs was used as a control. The cells in each experimental well were exposed to 808 nm laser irradiation (1 W/cm^2) for 5 min, and control samples were exposed to laser irradiation. Cell viability was determined using the CCK assay.

For Hoechst 33342/propidium iodide (PI) staining, MCF-7 cells (10^5 cells/well) were incubated in 6-well plates at 37 °C with 0.5 mg/mL Fe_3O_4/ICG@PLGA/PFP NPs and then irradiated by the NIR laser (808 nm, 1 W/cm^2) for 5 min. The cells were stained with a mixed solution of Hoechst 33342 and PI at 4 °C for 30 min and

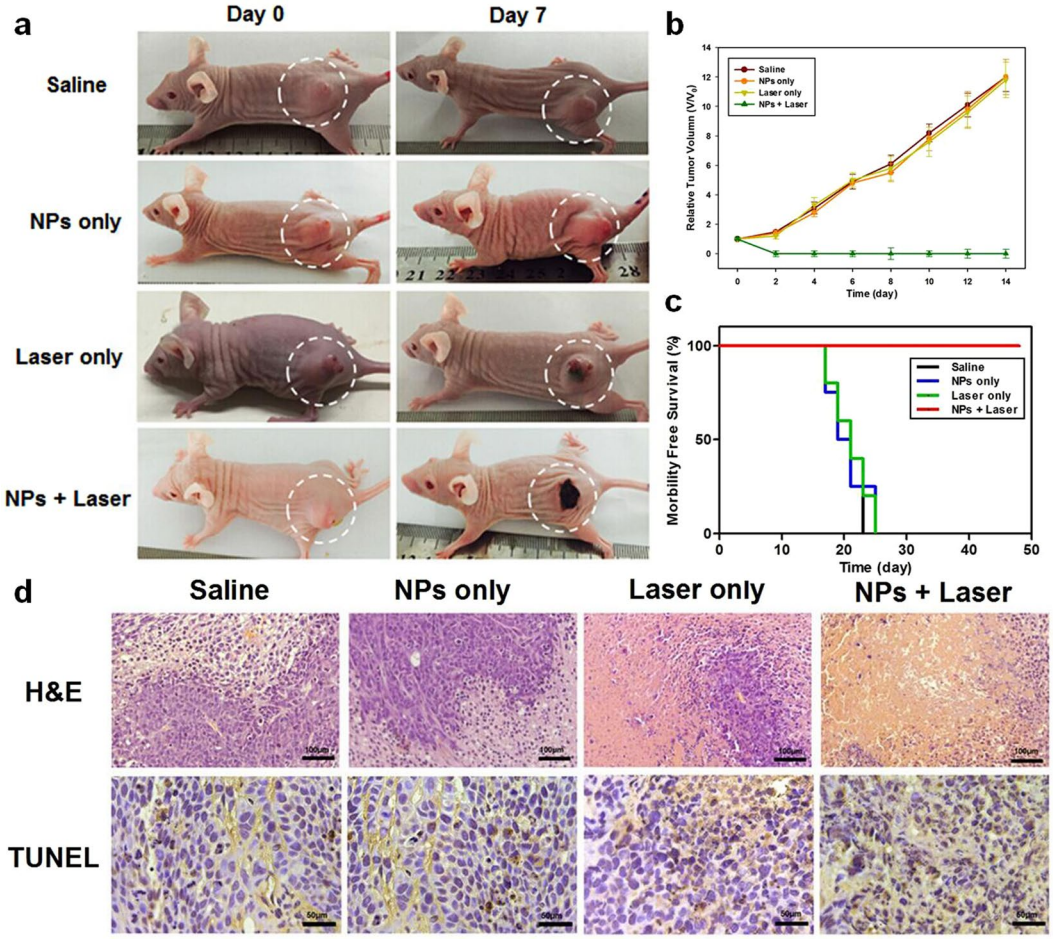

Figure 6. *In vivo* cancer therapy. (**a**) Representative photographs of mice from different groups at day 0 before treatment and at day 7 after treatment. (**b**) Tumor growth curves of mice after different treatments indicated. (**c**) Morbidity-free survival data after different treatments. (**d**) H&E and TUNEL staining of sections of tumors harvested 1 day after the different treatments. (H&E staining: 100×; scale bar, 100 μm; TUNEL staining: 200×; scale bar, 50 μm).

examined under a fluorescence microscope (Olympus IX71, Japan) to verify the photothermal effect on the cancer cells. The excitation wavelength was set at 355 nm for Hoechst 33342 and 545 nm for PI.

***In vivo* PTT.** Female BALB/c nude mice (20 g, age: 6–8 weeks) were obtained from the Medical Experimental Animal Center of the Second Xiangya Hospital of Central South University (Changsha, China). Animals received care in accordance with the Guidance Suggestions of the Ethics Committee of the Second Xiangya Hospital of Central South University in China. To establish the animal breast tumor model, 1×10^6 MCF-7 cells were administered by subcutaneous injection into the right flank of the nude mice.

When tumor volumes reached about 60 mm^3, mice were randomly divided into four treatment groups (n = 6 per group): (I) saline; (II) Fe_3O_4/ICG@PLGA/PFP NPs alone without laser irradiation (NPs only); (III) laser irradiation only without Fe_3O_4/ICG@PLGA/PFP NPs (laser only); and (IV) Fe_3O_4/ICG@PLGA/PFP NPs combined with laser irradiation (NPs + laser). In groups I, II, and IV, the nude mice received an intratumor injection of 50 μL saline or Fe_3O_4/ICG@PLGA/PFP NPs (2 mg/mL). Two hours after injection, the tumors of mice in groups III (laser only) and IV (NPs + laser) were irradiated with the 808 nm laser at a power density of 1.0 W/cm^2 for 5 min. The mice in groups I (saline) and II (NPs only) received no laser irradiation as controls. The temperature changes in the tumors were monitored by an infrared thermal imaging camera (Ti27, Fluke, USA). The tumor volume was calculated according to the formula: (tumor width)^2 × (tumor length)/2. The tumor size in each mouse was recorded every 2 days for 14 days.

One day after the different treatments, tumor tissues were harvested and evaluated via hematoxylin and eosin (H&E) staining, TdT-mediated dUTP nick end labeling (TUNEL) staining, and TEM examination for assessment of therapeutic efficacy.

Biological toxicity assessment. For assessment of the biological toxicity of the developed NPs, 10 healthy female BALB/c nude mice were intravenously injected with 0.2 mL of 2 mg/mL Fe_3O_4/ICG@PLGA/PFP NPs. Five additional mice were injected with saline as controls. Blood samples were collected for serum biochemistry

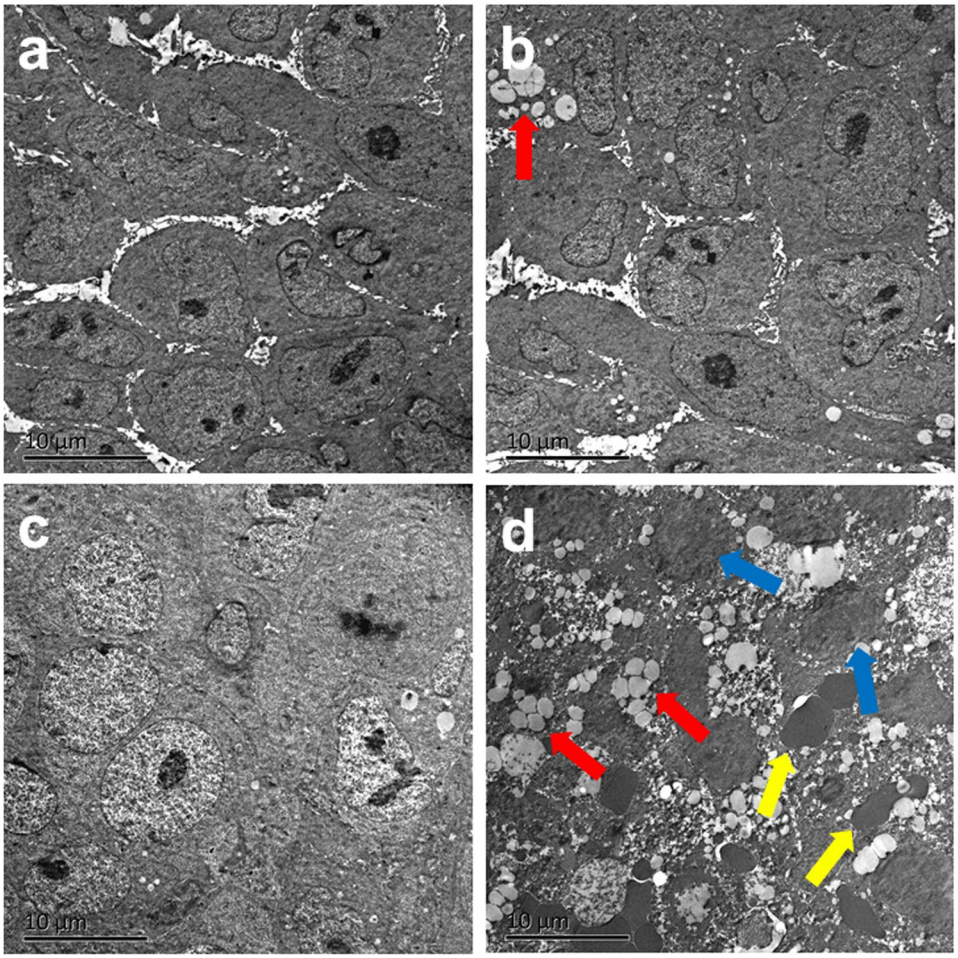

Figure 7. TEM images of tumor tissues from different treatment groups. (**a**) Saline; (**b**) Fe_3O_4/ICG@PLGA/PFP NPs only; (**c**) laser irradiation only; and (**d**) Fe_3O_4/ICG@PLGA/PFP NPs with laser irradiation. Magnification: 1450×; scale bar, 10 μm. Many generated microbubbles (red arrows) appeared in the tumor tissues. Blue arrows indicate interrupted cells, and yellow arrows indicate red blood cells.

assays at 3 and 14 days after injection of Fe_3O_4/ICG@PLGA/PFP NPs. After sacrifice at the final time point, the major organs including the liver, spleen, kidney, heart, lung and brain were harvested, and sections were stained with H&E.

Statistical analysis. All data are presented as means ± standard deviation (SD). Analysis of variance was used to analyze the data. Differences were considered significant if $p < 0.05$.

Results and Discussion

Structural characterization of Fe_3O_4/ICG@PLGA/PFP NPs. The Fe_3O_4/ICG@PLGA/PFP NPs were fabricated using our previously published method with a small change in the continuous sonication time from 40 s to 1 min[47]. The morphology and structure of Fe_3O_4/ICG@PLGA/PFP NPs were characterized by SEM and TEM. The Fe_3O_4/ICG@PLGA/PFP NPs appeared well dispersed and spherical in shape with a smooth surface morphology (Fig. 2a,b), average diameter of 289.6 ± 67.4 nm, and polydispersity index of 0.028 (Fig. 2d). In TEM (Fig. 2c), scattered black spots with diameter of 10 nm were clearly observed on the shells of Fe_3O_4/ICG@PLGA/PFP NPs, confirming the encapsulation of Fe_3O_4 NPs in the Fe_3O_4/ICG@PLGA/PFP NPs. Furthermore, the amount of Fe_3O_4 NPs encapsulated in the Fe_3O_4/ICG@PLGA/PFP NPs was determined by atomic absorption spectrometry to be 113.55 ± 3.12 μg/mL. The encapsulation efficiency of ICG was 45.53% ± 1.61% as measured by steady state spectrophotometry. The UV-Vis-NIR absorption spectra of Fe_3O_4/ICG@PLGA/PFP NPs, ICG, and Fe_3O_4 NPs displayed strong absorption in PBS in the range of 400–900 nm (Fig. 2e). The spectrum of Fe_3O_4 NPs exhibited no obvious peak, whereas that of free ICG had a peak around 770~790 nm. The absorption spectrum of Fe_3O_4/ICG@PLGA/PFP NPs displayed a small peak around 790~810 nm with an obvious red shift, which is consistent with previously published results for ICG[33,57–61], confirming that ICG was successfully encapsulated in the NPs. The observed absorbance in the NIR region verified that the Fe_3O_4/ICG@PLGA/PFP NPs could serve as a good photo-absorbing agent for tumor PTT.

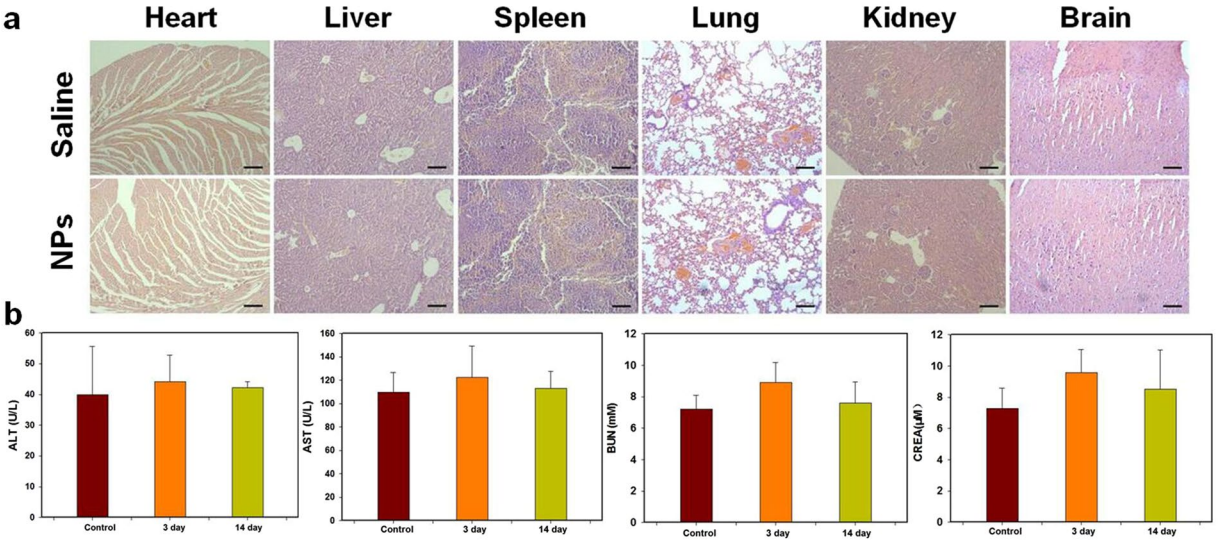

Figure 8. *In vivo* toxicity study. (**a**) H&E stained sections of major organs harvested 14 days after intravenous injection of 0.2 mL of 2 mg/mL Fe_3O_4/ICG@PLGA/PFP NPs or saline as the control. No noticeable abnormality was observed in the heart, liver, spleen, lung, kidney, or brain. (**b**) Levels of hepatic functional markers (ALT and AST) and renal functional markers (BUN and CREA) in the blood at 3 and 14 days after injection of Fe_3O_4/ICG@PLGA/PFP NPs or saline as the control.

***In vitro* PTT effect of Fe_3O_4/ICG@PLGA/PFP NPs.** To study the effectiveness of using Fe_3O_4/ICG@PLGA/PFP NPs in PTT, aqueous suspensions of Fe_3O_4/ICG@PLGA/PFP NPs, mixture of ICG and Fe_3O_4 NPs, free ICG, Fe_3O_4 NPs, and PBS were exposed to 808 nm NIR laser irradiation with a power density of 1.0 W/cm^2 for 10 min. The rapidly increasing temperature of Fe_3O_4/ICG@PLGA/PFP NPs allowed them to act as an effective photothermal nanoagent for PTT. As shown in Fig. 3a, no obvious temperature change was observed when PBS was exposed to NIR laser irradiation. In contrast, under the same concentration (0.2 mL solution with 5 μg/mL ICG or 113 μg/mL Fe) and laser irradiation conditions, the maximum temperatures achieved in the free ICG, Fe_3O_4 NPs, mixture of ICG and Fe_3O_4 NPs, and Fe_3O_4/ICG@PLGA/PFP NP solutions were 52.8 °C, 43.2 °C, 57.0 °C, and 57.9 °C, respectively. The higher maximum temperature observed for the Fe_3O_4/ICG@PLGA/PFP NPs and the mixture of ICG and Fe_3O_4 NPs indicates that Fe_3O_4/ICG@PLGA/PFP NPs and the combination of ICG and Fe_3O_4 NPs may be more effective than pure ICG or Fe_3O_4 NPs in PTT. This result indicates that both the ICG and Fe_3O_4 NPs entrapped in the Fe_3O_4/ICG@PLGA/PFP NPs contribute to the NIR-dependent temperature increase and that Fe_3O_4/ICG@PLGA/PFP NPs could act as efficient NIR light absorbers for PTT.

To compare the photostability of Fe_3O_4/ICG@PLGA/PFP NPs with that of the free ICG molecules, solutions of Fe_3O_4/ICG@PLGA/PFP NPs, ICG@PLGA/PFP NPs and ICG were irradiated with the NIR laser for 3 min (Laser ON), followed by natural cooling for 10 min (Laser OFF). After each of the four laser ON/OFF cycles, as shown in Fig. 3b, the temperature increases in the Fe_3O_4/ICG@PLGA/PFP NPs solution were 25.1 °C, 23.2 °C, 21.3 °C and 20.1 °C; the temperature increases in the ICG@PLGA/PFP NP solution were 21.1 °C, 19.2 °C, 17.3 °C, and 16.1 °C; and those for the free ICG solution were 20.3 °C, 10.5 °C, 8.3 °C, and 6.3 °C. The greater increase in the temperature of the ICG@PLGA/PFP NP solution indicated that ICG loaded in the polymeric layers NPs show greater photostability than the free ICG molecules. The temperature increases in the Fe_3O_4/ICG@PLGA/PFP NP solution were greater than those in the ICG@PLGA/PFP NP solution, which showed that Fe_3O_4 in the former NPs also contributed to the photothermal conversion efficiency. This result is consistent with the findings of a previous study by Dai *et al.*[1] concerning lipid shell NPs.

***In vitro* cytotoxicity of Fe_3O_4/ICG@PLGA/PFP NPs.** To investigate the photothermal cytotoxicity of Fe_3O_4/ICG@PLGA/PFP NPs, MCF-7 cells were incubated with various concentrations of Fe_3O_4/ICG@PLGA/PFP NPs for 6 h and then treated with or without 808 nm laser irradiation at a power density of 1.0 W/cm^2 for 5 min before cell viability was measured via CCK-8 assay. Cells not exposed to NPs and irradiated or not served as the controls. As shown in Fig. 4a, no obvious decrease in cell viability was observed upon exposure to various concentrations of Fe_3O_4/ICG@PLGA/PFP NPs without laser irradiation. In contrast, enhanced cancer cell ablation was observed with increasing concentrations of Fe_3O_4/ICG@PLGA/PFP NPs under NIR laser irradiation.

To further confirm the photothermal effect of Fe_3O_4/ICG@PLGA/PFP NPs, viable and dead cells within MCF-7 cell samples were stained with Hoechst 33342 and PI, respectively. As shown in Fig. 4b, many dead cells (red fluorescent) were observed only after treatment with both Fe_3O_4/ICG@PLGA/PFP NPs and laser irradiation, indicating that some cells underwent photothermal destruction. In comparison, samples from the control groups showed blue staining over the entire area, suggesting that treatment with Fe_3O_4/ICG@PLGA/PFP NPs or laser irradiation alone did not induce cell death. These results demonstrate that the Fe_3O_4/ICG@PLGA/PFP NPs could effectively kill the tumor cells through PTT only upon NIR laser irradiation.

Use of Fe_3O_4/ICG@PLGA/PFP NPs in PTT for tumor ablation *in vivo*. To further study the potential of Fe_3O_4/ICG@PLGA/PFP NPs for *in vivo* cancer PTT, mice bearing MCF-7 cell tumors were subjected to four different treatments: saline, Fe_3O_4/ICG@PLGA/PFP NPs only, laser irradiation only, Fe_3O_4/ICG@PLGA/PFP NPs and laser irradiation. As monitored by an infrared thermal camera, the temperature of tumor tissue injected with Fe_3O_4/ICG@PLGA/PFP NPs increased rapidly from 32.2 °C to 52.3 °C under laser irradiation. In contrast, no temperature increases were observed in tumors after treatment with saline, NPs only, or laser irradiation only (Fig. 5a and b).

The photographs in Fig. 6a show the black scars that appeared over the sites of tumors injected with Fe_3O_4/ICG@PLGA/PFP NPs upon laser irradiation. In these mice, the tumor size declined significantly, and the scar tissue gradually fell off within 14 days laser irradiation. However, in the three control groups treated with saline only, NPs only, or laser irradiation only, the volumes of tumors increased by more than 12-fold from day 0 to day 14 after treatment (Fig. 6b). Moreover, mice in the three control groups showed a survival range of 17–23 days after treatment, whereas all mice treated with Fe_3O_4/ICG@PLGA/PFP NP injection and laser irradiation remained alive at 48 days after treatment with complete tumor ablation achieved by PTT (Fig. 6c). These results demonstrate that Fe_3O_4/ICG@PLGA/PFP NPs could effectively inhibit tumor growth via their photothermal efficacy.

The therapeutic effectiveness of Fe_3O_4/ICG@PLGA/PFP NPs in PTT was also investigated by H&E staining, TUNEL staining, and TEM examination of tumor tissues harvested from the different groups of mice 1 day after treatment. H&E staining revealed severe damage with coagulative necrosis, leaving a mass of red-stained substance in tumor tissue injected with NPs and exposed to laser irradiation. Comparatively, no notable damage was found in the three control groups (Fig. 6d). TUNEL staining further verified the presence of many more necrotic cells in tumor tissues of mice treated with the NPs and laser irradiation than in tumor tissues of the other three groups, demonstrating the greater damage to tumor cells achieved via the photothermal effect of Fe_3O_4/ICG@PLGA/PFP NPs (Fig. 6d). In addition, on TEM images, coagulative necrosis was more evident in the tumor tissues of mice treated with the NPs and laser irradiation than in that of the other three groups, which was consistent with our H&E staining results (Fig. 7). In the representative image showed in Fig. 7d, after treatment with NPs and laser irradiation, no clear cell structure could be distinguished, most cell membranes and nuclear membranes had ruptured or disintegrated (indicated by blue arrows), organelles had disappeared, and only remnants of the nuclear shadow remained. Moreover, the tumor blood vessels had ruptured, resulting in leakage of red blood cells. Comparatively, in the three control groups, the tumor tissue retained the original structure with no obvious damage (Fig. 7a–c). Finally, many microbubbles (red arrows) appeared in the tumor tissues treated with NPs and laser irradiation, with Fe particles expelled to the edge or outside of the microbubbles (Fig. 7d). This revealed that most Fe_3O_4/ICG@PLGA/PFP NPs absorbed the light energy and converted it into heat upon laser irradiation, and the PFP in the NPs underwent a phase shift to form microbubbles. In tumor tissues treated with NPs only without laser irradiation, only a small portion of NPs produced microbubbles (Fig. 7b). We think this may have occurred after harvesting of the tissue during the heated polymerization process of the TEM sample operation, when a temperature exceeding 70 °C is commonly used; at such temperatures, some of the NPs in the excised tissues could absorb the heat, resulting in microbubble formation.

***In vivo* toxicity of Fe3O4/ICG@PLGA/PFP NPs.** To further assess the *in vivo* toxicity of Fe_3O_4/ICG@PLGA/PFP NPs, major organs (heart, liver, spleen, lung, kidney, and brain) of healthy BABL/c mice injected with Fe_3O_4/ICG@PLGA/PFP NPs (0.2 mL, 2 mg/mL) via the tail vein were harvested,sectioned, and stained with H&E for histological analysis at 14 days post-injection. In addition, blood samples of these healthy BABL/c mice were collected and analyzed at 3 and 14 days post-injection. No noticeable organ damage or inflammatory lesion were observed in H&E stained sections of major organs from mice treated with Fe_3O_4/ICG@PLGA/PFP NPs, indicating that the Fe_3O_4/ICG@PLGA/PFP NPs did not induce appreciable toxic side effects in treated animals (Fig. 8a). Moreover, two indicators of hepatic function, alanine aminotransferase (ALT) and aspartate aminotransferase (AST) levels, and two indicators of renal function, urea nitrogen (UREA) and creatinine (CREA) levels, were measured in blood samples from NP-treated mice. As shown in Fig. 8b, the levels of these four indicators were within normal ranges with no significant differences between the different time points (all $^*p < 0.05$). Thus, the histological examination and serum biochemistry results indicate that Fe_3O_4/ICG@PLGA/PFP NPs at the tested dose have no cytotoxic effects in healthy mice in the absence of laser irradiation.

Conclusion

The multifunctional Fe_3O_4/ICG@PLGA/PFP NPs synthesized in this study showed promising results as a photothermal agent for cancer treatment. The photo-absorbance by Fe_3O_4 NPs and ICG co-embedded in the Fe_3O_4/ICG@PLGA/PFP NP shell, along with the microbubbles generated upon the liquid-gas phase shift of PFP encapsulated in the NPs process make it possible to achieve photothermal tumor therapy. This successful demonstration of the use of nanobiotechnology for NIR laser-induced PTT provides an alternative modality for effective nanotheranostics.

References

1. Ma, Y., Tong, S., Bao, G., Gao, C. & Dai, Z. Indocyanine green loaded SPIO nanoparticles with phospholipid-PEG coating for dual-modal imaging and photothermal therapy. *Biomaterials* **34**, 7706–7714 (2013).
2. Shen, S. *et al*. Magnetic nanoparticle clusters for photothermal therapy with near-infrared irradiation. *Biomaterials* **39**, 67–74 (2015).
3. Sun, Y. *et al*. Superparamagnetic PLGA-iron oxide microcapsules for dual-modality US/MR imaging and high intensity focused US breast cancer ablation. *Biomaterials* **33**, 5854–5864 (2012).
4. Sun, Y. *et al*. Evaluation of superparamagnetic iron oxide-polymer composite microcapsules for magnetic resonance-guided high-intensity focused ultrasound cancer surgery. *BMC Cancer* **14**, 800 (2014).
5. Ke, H. *et al*. Gold nanoshelled liquid perfluorocarbon magnetic nanocapsules: a nanotheranostic platform for bimodal ultrasound/magnetic resonance imaging guided photothermal tumor ablation. *Theranostics* **4**, 12–23 (2013).

6. Wang, Y. *et al*. Comparison study of gold nanohexapods, nanorods, and nanocages for photothermal cancer treatment. *ACS Nano* **7**, 2068–2077 (2013).
7. Li, Z. *et al*. Small gold nanorods laden macrophages for enhanced tumor coverage in photothermal therapy. *Biomaterials* **74**, 144–154 (2016).
8. Qin, J. *et al*. Gold nanorods as a theranostic platform for *in vitro* and *in vivo* imaging and photothermal therapy of inflammatory macrophages. *Nanoscale* **7**, 13991–14001 (2015).
9. Arunkumar, P. *et al*. Near infra-red laser mediated photothermal and antitumor efficacy of doxorubicin conjugated gold nanorods with reduced cardiotoxicity in swiss albino mice. *Nanomedicine* **11**, 1435–1444 (2015).
10. Kaneti, Y. V. *et al*. Carbon-Coated Gold Nanorods: A Facile Route to Biocompatible Materials for Photothermal Applications. *ACS Appl Mater Interfaces* **7**, 25658–2566 (2015).
11. Piao, J. G. *et al*. Erythrocyte membrane is an alternative coating to polyethylene glycol for prolonging the circulation lifetime of gold nanocages for photothermal therapy. *ACS Nano* **8**, 10414–10425 (2014).
12. Huang, X., El-Sayed, I. H., Qian, W. & El-Sayed, M. A. Cancer cell imaging and photothermal therapy in the near-infrared region by using gold nanorods. *J Am Chem Soc* **128**, 2115–2120 (2006).
13. Feng, Q. *et al*. Tumor-targeted and multi-stimuli responsive drug delivery system for near-infrared light induced chemo-phototherapy and photoacoustic tomography. *Acta Biomater* **38**, 129–142 (2016).
14. Li, K. C., Chu, H. C., Lin, Y., Tuan, H. Y. & Hu, Y. C. PEGylated Copper Nanowires as a Novel Photothermal Therapy Agent. *ACS Appl Mater Interfaces* **8**, 12082–12090 (2016).
15. Wang, S. *et al*. Plasmonic copper sulfide nanocrystals exhibiting near-infrared photothermal and photodynamic therapeutic effects. *ACS Nano* **9**, 1788–1800 (2015).
16. Liu, R. *et al*. Manganese (II) Chelate Functionalized Copper Sulfide Nanoparticles for Efficient Magnetic Resonance/Photoacoustic Dual-Modal Imaging Guided Photothermal Therapy. *Theranostics* **5**, 1144–1153 (2015).
17. Guo, L. *et al*. Combinatorial photothermal and immuno cancer therapy using chitosan-coated hollow copper sulfide nanoparticles. *ACS Nano* **8**, 5670–5681 (2014).
18. Li, Y. *et al*. Copper sulfide nanoparticles for photothermal ablation of tumor cells. *Nanomedicine (Lond)* **5**, 1161–1171 (2010).
19. Wang, S. *et al*. Manganese Oxide-Coated Carbon Nanotubes As Dual-Modality Lymph Mapping Agents for Photothermal Therapy of Tumor Metastasis. *ACS Appl Mater Interfaces* **8**, 3736–3743 (2016).
20. Zhang, P. *et al*. Noncovalent Ruthenium(II) Complexes-Single-Walled Carbon Nanotube Composites for Bimodal Photothermal and Photodynamic Therapy with Near-Infrared Irradiation. *ACS Appl Mater Interfaces* **7**, 23278–23290 (2015).
21. Whitney, J. *et al*. 3D viability imaging of tumor phantoms treated with single-walled carbon nanohorns and photothermal therapy. *Nanotechnology* **24**, 275102 (2013).
22. Rossella, F., Soldano, C., Bellani, V. & Tommasini, M. Metal-filled carbon nanotubes as a novel class of photothermal nanomaterials. *Adv Mater* **24**, 2453–2458 (2012).
23. Chu, M. *et al*. Laser light triggered-activated carbon nanosystem for cancer therapy. *Biomaterials* **34**, 1820–1832 (2013).
24. Guo, F., Yu, M., Wang, J., Tan, F. & Li, N. Smart IR780 Theranostic Nanocarrier for Tumor-Specific Therapy: Hyperthermia-Mediated Bubble-Generating and Folate-Targeted Liposomes. *ACS Appl Mater Interfaces* **7**, 20556–20567 (2015).
25. Yue, C. *et al*. IR-780 dye loaded tumor targeting theranostic nanoparticles for NIR imaging and photothermal therapy. *Biomaterials* **34**, 6853–6861 (2013).
26. Yuan, A. *et al*. Self-assembled PEG-IR-780-C13 micelle as a targeting, safe and highly-effective photothermal agent for *in vivo* imaging and cancer therapy. *Biomaterials* **51**, 184–193 (2015).
27. Jiang, C. *et al*. Hydrophobic IR780 encapsulated in biodegradable human serum albumin nanoparticles for photothermal and photodynamic therapy. *Acta Biomater* **14**, 61–69 (2015).
28. Pokhrel, S., Nel, A. E. & Madler, L. Custom-designed nanomaterial libraries for testing metal oxide toxicity. *Acc Chem Res* **46**, 632–641 (2013).
29. Nel, A. *et al*. Nanomaterial toxicity testing in the 21st century: use of a predictive toxicological approach and high-throughput screening. *Acc Chem Res* **46**, 607–621 (2013).
30. Andon, F. T. & Fadeel, B. Programmed cell death: molecular mechanisms and implications for safety assessment of nanomaterials. *Acc Chem Res* **46**, 733–742 (2013).
31. Alander, J. T. *et al*. A review of indocyanine green fluorescent imaging in surgery. *Int J Biomed Imaging* **2012**, 940585 (2012).
32. Malicka, J., Gryczynski, I., Geddes, C. D. & Lakowicz, J. R. Metal-enhanced emission from indocyanine green: a new approach to *in vivo* imaging. *J Biomed Opt* **8**, 472–478 (2003).
33. Kirchherr, A. K., Briel, A. & Mader, K. Stabilization of indocyanine green by encapsulation within micellar systems. *Mol Pharm* **6**, 480–491 (2009).
34. Saxena, V., Sadoqi, M. & Shao, J. Degradation kinetics of indocyanine green in aqueous solution. *J Pharm Sci* **92**, 2090–2097 (2003).
35. Saxena, V., Sadoqi, M. & Shao, J. Polymeric nanoparticulate delivery system for Indocyanine green: biodistribution in healthy mice. *Int J Pharm* **308**, 200–204 (2006).
36. Saxena, V., Sadoqi, M. & Shao, J. Enhanced photo-stability, thermal-stability and aqueous-stability of indocyanine green in polymeric nanoparticulate systems. *J Photochem Photobiol B* **74**, 29–38 (2004).
37. Wang, L. *et al*. Indocyanine-green-loaded microbubbles for localization of sentinel lymph node using near-infrared fluorescence/ultrasound imaging: a feasibility study. *RSC Advances* **6**, 50513–50520 (2016).
38. Yan, F. *et al*. Molecular imaging-guided photothermal/photodynamic therapy against tumor by iRGD-modified indocyanine green nanoparticles. *J Control Release* **224**, 217–228 (2016).
39. Yu, J. *et al*. Self-assembly synthesis, tumor cell targeting, and photothermal capabilities of antibody-coated indocyanine green nanocapsules. *J Am Chem Soc* **132**, 1929–1938 (2010).
40. Chen, Q. *et al*. Photothermal therapy with immune-adjuvant nanoparticles together with checkpoint blockade for effective cancer immunotherapy. *Nat Commun* **7**, 13193 (2016).
41. Zhao, Y. *et al*. Phase-Shifted PFH@PLGA/Fe_3O_4 Nanocapsules for MRI/US Imaging and Photothermal Therapy with near-Infrared Irradiation. *ACS Appl Mater Interfaces* **7**, 14231–14242 (2015).
42. Zhou, Z. *et al*. Iron/iron oxide core/shell nanoparticles for magnetic targeting MRI and near-infrared photothermal therapy. *Biomaterials* **35**, 7470–7478 (2014).
43. McCarthy, J. R., Kelly, K. A., Sun, E. Y. & Weissleder, R. Targeted delivery of multifunctional magnetic nanoparticles. *Nanomedicine (Lond)* **2**, 153–167 (2007).
44. Wang, Y. X., Hussain, S. M. & Krestin, G. P. Superparamagnetic iron oxide contrast agents: physicochemical characteristics and applications in MR imaging. *Eur Radiol* **11**, 2319–2331 (2001).
45. Wu, M. *et al*. Nanocluster of superparamagnetic iron oxide nanoparticles coated with poly (dopamine) for magnetic field-targeting, highly sensitive MRI and photothermal cancer therapy. *Nanotechnology* **26**, 115102 (2015).
46. Zhang, L. *et al*. Imaging and cell targeting characteristics of magnetic nanoparticles modified by a functionalizable zwitterionic polymer with adhesive 3,4-dihydroxyphenyl-l-alanine linkages. *Biomaterials* **31**, 6582–6588 (2010).
47. Niu, C. *et al*. Doxorubicin loaded superparamagnetic PLGA-iron oxide multifunctional microbubbles for dual-mode US/MR imaging and therapy of metastasis in lymph nodes. *Biomaterials* **34**, 2307–231 (2013).

48. Kripfgans, O. D., Fowlkes, J. B., Miller, D. L., Eldevik, O. P. & Carson, P. L. Acoustic droplet vaporization for therapeutic and diagnostic applications. *Ultrasound Med Biol* **26**, 1177–1189 (2000).
49. Strohm, E., Rui, M., Gorelikov, I., Matsuura, N. & Kolios, M. Vaporization of perfluorocarbon droplets using optical irradiation. *Biomed Opt Express* **2**, 1432–1442 (2011).
50. Reznik, N., Williams, R. & Burns, P. N. Investigation of vaporized submicron perfluorocarbon droplets as an ultrasound contrast agent. *Ultrasound Med Biol* **37**, 1271–1279 (2011).
51. Zhang, M. *et al*. Initial investigation of acoustic droplet vaporization for occlusion in canine kidney. *Ultrasound Med Biol* **36**, 1691–1703 (2010).
52. Kripfgans, O. D., Fowlkes, J. B., Woydt, M., Eldevik, O. P. & Carson, P. L. *In vivo* droplet vaporization for occlusion therapy and phase aberration correction. *IEEE Trans Ultrason Ferroelectr Freq Control* **49**, 726–738 (2002).
53. Samuel, S., Duprey, A., Fabiilli, M. L., Bull, J. L. & Fowlkes, J. B. *In vivo* microscopy of targeted vessel occlusion employing acoustic droplet vaporization. *Microcirculation* **19**, 501–509 (2012).
54. Rapoport, N., Christensen, D. A., Kennedy, A. M. & Nam, K. H. Cavitation properties of block copolymer stabilized phase-shift nanoemulsions used as drug carriers. *Ultrasound Med Biol* **36**, 419–429 (2010).
55. Rapoport, N., Gao, Z. & Kennedy, A. Multifunctional nanoparticles for combining ultrasonic tumor imaging and targeted chemotherapy. *J Natl Cancer Inst* **99**, 1095–1106 (2007).
56. Rapoport, N. Y., Kennedy, A. M., Shea, J. E., Scaife, C. L. & Nam, K. H. Controlled and targeted tumor chemotherapy by ultrasound-activated nanoemulsions/microbubbles. *J Control Release* **138**, 268–276 (2009).
57. Sun, Y. *et al*. Laser-Activatible PLGA Microparticles for Image-Guided Cancer Therapy *In Vivo*. *Adv Funct Mater* **24**, 7674–7680 (2014).
58. Zhou, Y. *et al*. Microbubbles from gas-generating perfluorohexane nanoemulsions for targeted temperature-sensitive ultrasonography and synergistic HIFU ablation of tumors. *Adv Mater* **25**, 4123–4130 (2013).
59. Yan, L. & Qiu, L. Indocyanine green targeted micelles with improved stability for near-infrared image-guided photothermal tumor therapy. *Nanomedicine (Lond)* **10**, 361–373 (2015).
60. Zheng, X., Zhou, F., Wu, B., Chen, W. R. & Xing, D. Enhanced tumor treatment using biofunctional indocyanine green-containing nanostructure by intratumoral or intravenous injection. *Mol Pharm* **9**, 514–522 (2012).
61. Zheng, X., Xing, D., Zhou, F., Wu, B. & Chen, W. R. Indocyanine green-containing nanostructure as near infrared dual-functional targeting probes for optical imaging and photothermal therapy. *Mol Pharm* **8**, 447–456 (2011).

Acknowledgements

The authors thank Zhigang Wang and Pan Li (Chongqing Medical University) for their technical assistance. This project was funded by the National Natural Science Foundation of China (Grant No. 81401431, 81201096, 81672138, and 81601883), and Hunan Provincial Natural Science Foundation of China (Grant No. 2017JJ3443).

Author Contributions

Q.H.P. and C.C.N. conceptualized the experiments, designed and directed the experiments, and edited the manuscript. C.C.N. and L.W. designed and performed the *in vitro* experiments and wrote the manuscript. Y.X. and S.B.A carried the *in vivo* experiments. Z.M. and Y.H.H. oversaw research activities and the experiments.

Additional Information

Competing Interests: The authors declare that they have no competing interests.

Publisher's note: Springer Nature remains neutral with regard to jurisdictional claims in published maps and institutional affiliations.